HOKKAIDO UNIVERSITY

Title	Fabrication of Epitaxial Fe3O4 Film on a Si(111) Substrate
Author(s)	Takahashi, Nozomi; Huminiuc, Teodor; Yamamoto, Yuta; Yanase, Takashi; Shimada, Toshihiro; Hirohata, Atsufumi; Nagahama, Taro
Citation	Scientific reports, 7, 7009 https://doi.org/10.1038/s41598-017-07104-z
Issue Date	2017-08-01
Doc URL	http://hdl.handle.net/2115/67151
Rights(URL)	https://creativecommons.org/licenses/by/4.0/
Type	article
File Information	s41598-017-07104-z.pdf

Instructions for use

SCIENTIFIC REPORTS

OPEN

Fabrication of Epitaxial Fe$_3$O$_4$ Film on a Si(111) Substrate

Nozomi Takahashi[1], Teodor Huminiuc[2], Yuta Yamamoto[1], Takashi Yanase[3], Toshihiro Shimada[3], Atsufumi Hirohata[4] & Taro Nagahama[3]

The application of magnetic oxides in spintronics has recently attracted much attention. The epitaxial growth of magnetic oxide on Si could be the first step of new functional spintronics devices with semiconductors. However, epitaxial spinel ferrite films are generally grown on oxide substrates, not on semiconductors. To combine oxide spintronics and semiconductor technology, we fabricated Fe$_3$O$_4$ films through epitaxial growth on a Si(111) substrate by inserting a γ-Al$_2$O$_3$ buffer layer. Both of γ-Al$_2$O$_3$ and Fe$_3$O$_4$ layer grew epitaxially on Si and the films exhibited the magnetic and electronic properties as same as bulk. Furthermore, we also found the buffer layer dependence of crystal structure of Fe$_3$O$_4$ by X-ray diffraction and high-resolution transmission electron microscope. The Fe$_3$O$_4$ films on an amorphous-Al$_2$O$_3$ buffer layer grown at room temperature grew uniaxially in the (111) orientation and had a textured structure in the plane. When Fe$_3$O$_4$ was deposited on Si(111) directly, the poly-crystal Fe$_3$O$_4$ films were obtained due to SiO$_x$ on Si substrate. The epitaxial Fe$_3$O$_4$ layer on Si substrates enable us the integration of highly functional spintoronic devices with Si technology.

In the field of spintronics, spin injection and transport phenomena have attracted much attention owing to the possibility of producing novel functional devices[1–3]. In particular, the combination of spintronics and semiconductors is a promising technology for the development of the next stage of spintronic devices, e.g., spin-FET or logic devices[4, 5]. The spin injection technique, in which the spin-polarized currents are injected from ferromagnetic metals into conventional semiconductor materials[2, 3, 6], has been intensely investigated for the preparation of spintronic devices. As a result, researchers have succeeded in nonlocal detection[7] or the observation of the Hanle effect[1], which demonstrates the spin state in the semiconductor; thus, the behavior of the spin current in the semiconductor can be determined[8]. Recently, graphene has also been the subject of spin injection because the spin diffusion length in such light elements is expected to be long owing to small spin–orbit interaction[9, 10].

The source of the spin current plays an important role in obtaining high-efficiency spin injection. Magnetic oxides are one of the most promising spin source candidates. However, ferromagnetic metals have been used so far because of convenience during fabrication. Magnetic oxides possess unique properties[11–14]; Fe$_3$O$_4$ or (LaSr) MnO$_3$ have a half-metallic state, which provides highly spin polarized current[15], and NiFe$_2$O$_4$ or CoFe$_2$O$_4$ are magnetic insulators, which means that they could work as a spin filter tunnel barrier[16–18]. γ-Fe$_2$O$_3$ is another candidate as the spin filter barrier. It is the spinel type ferrimagnetic insulator that is obtained by over oxidation of Fe$_3$O$_4$[19]. Recently, NiCo$_2$O$_4$ with spinel structure was discovered to exhibit large magnetoresistance effects[20]. Therefore, the combination of magnetic oxides and semiconductors enables us to produce new functional devices. Some research groups fabricated the magnetic oxide on oxide semiconductor, Nb:SrTiO$_3$, and investigated the transport characteristics including spin transport of the junctions[19, 21]. However, epitaxial growth of magnetic oxide on Si, which is the most important semiconductor, has not been established because the surface of Si is easily oxidized by the oxygen atmosphere during the evaporation of the magnetic oxides[22].

In this study, we grew Fe$_3$O$_4$ epitaxially on a Si(111) substrate by the insertion of an ultrathin γ-Al$_2$O$_3$ buffer layer. Fe$_3$O$_4$ is the ferrimagnetic conducting oxide with spinel crystal structure. At 120K, Fe$_3$O$_4$ shows phase transition called Verwey transition, at which the electric resistivity increases drastically and the crystal symmetry decreases from face-centered cubic to monoclinic[23–25]. Fe$_3$O$_4$ is expected to be half-metallic theoretically, meaning to have a spin polarization of 100%[15], and a spin polarization of more than 80% was observed experimentally using a spin-resolved photoemission spectroscopy[26]. An ultrathin γ-Al$_2$O$_3$ layer was inserted to prevent surface

[1]Graduate School of Chemical Sciences and Engineering, Hokkaido University, Sapporo, 060-8628, Japan. [2]Department of Physics, University of York, Heslington, York, YO10 5DD, England. [3]Graduate School of Engineering, Hokkaido University, Sapporo, 060-8628, Japan. [4]Department of Electronic Engineering, University of York, Heslington, York, YO10 5DD, England. Correspondence and requests for materials should be addressed to T.N. (email: nagahama@eng.hokudai.ac.jp)
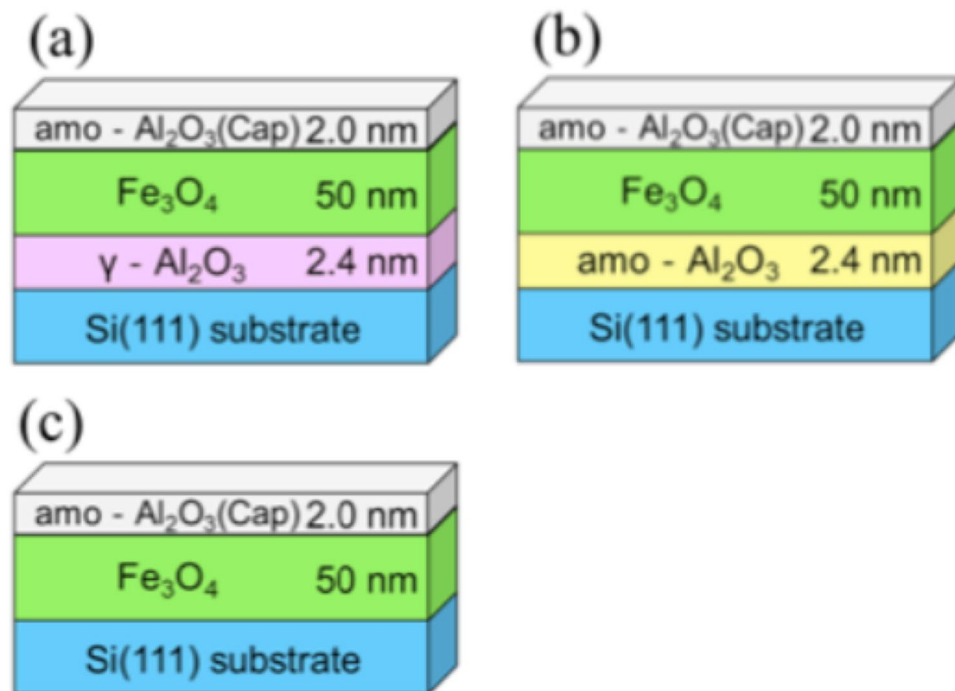
Figure 1. Sample structures: (**a**) the sample with γ-Al$_2$O$_3$ buffer layer (EPI), (**b**) with amorphous-Al$_2$O$_3$ buffer layer (AMO), and (**c**) without a buffer layer (W/O).

oxidation of Si during the Fe$_3$O$_4$ growth. γ-Al$_2$O$_3$ is an aluminum oxide with the same spinel structure as Fe$_3$O$_4$ and the lattice constant of γ-Al$_2$O$_3$ is 7.91 Å, which is three halves of that of Si with lattice mismatch of -2.9%[27]. From the viewpoint of the crystal structure, Fe$_3$O$_4$ and γ-Al$_2$O$_3$ seems to grow on Si epitaxially.

γ-Al$_2$O$_3$ (111) epitaxial growth on Si(111) was reported by two research groups recently. Jung *et al.* formed a γ-Al$_2$O$_3$ (111) layer by annealing an Al layer on protective Si oxide, which was carefully oxidized to be reduced by the Al layer[28]. Merckling *et al.* fabricated γ-Al$_2$O$_3$ (111) by the deposition of an Al$_2$O$_3$ source under ultra-high vacuum[29]. In the former method, it is difficult to optimize the oxidation of the Si layer and the thickness of Al film. In contrast, the latter method is simple if an ultra-high vacuum system is accessible.

In this study, the epitaxial γ-Al$_2$O$_3$ buffer layers were prepared using an ultra-high vacuum system and the Fe$_3$O$_4$ layer was fabricated by reactive molecular beam epitaxy. We investigated the crystal structure, magnetic and electric properties of the Fe$_3$O$_4$ layer on Si(111) with an epitaxial γ-Al$_2$O$_3$ buffer layer, an amorphous-Al$_2$O$_3$ buffer layer, and without a buffer layer. We succeeded in the fabrication of high quality Fe$_3$O$_4$ films on Si(111) substrates. The buffer layer had a significant effect on the crystal structure of the Fe$_3$O$_4$ layers.

Results and Discussion

Epitaxial growth. The γ-Al$_2$O$_3$ and Fe$_3$O$_4$ layers were grown by molecular beam epitaxy method. The structures of the samples were (a) Si(111)/γ-Al$_2$O$_3$ 2.4 nm/Fe$_3$O$_4$ 50 nm/amorphous-Al$_2$O$_3$ 2.0 nm, (b) Si(111)/amorphous-Al$_2$O$_3$ 2.4 nm/Fe$_3$O$_4$ 50 nm/amorphous-Al$_2$O$_3$ 2.0 nm and (c) Si(111)/Fe$_3$O$_4$ 50 nm/amorphous-Al$_2$O$_3$ 2.0 nm, as shown in Fig. 1 (hereafter referred to as (a) EPI, (b) AMO and (c) W/O), respectively. After treatment of the Si substrate, we confirmed that the *in-situ* reflection high energy electron diffraction (RHEED) pattern of the Si substrate had a (7×7) streak pattern (Supplementary Fig. S1). This means that the surface of Si was clean and flat. Figure 2(a) and (b) show the RHEED pattern of γ-Al$_2$O$_3$ and Fe$_3$O$_4$ in EPI. The direction of the incident electron beam was [11-2]. The RHEED patterns of γ-Al$_2$O$_3$ and Fe$_3$O$_4$ were clear streak patterns indicating that γ-Al$_2$O$_3$ and Fe$_3$O$_4$ grew epitaxially. Therefore, the γ-Al$_2$O$_3$ film was considered to play a role of a buffer layer for epitaxial growth of Fe$_3$O$_4$. The surface roughness of γ-Al$_2$O$_3$ and Fe$_3$O$_4$ were estimated to be very small in value by atomic force microscopy (AFM) (shown in Supplementary Fig. S2).

Figure 2(c) and (d) show the RHEED pattern of amorphous-Al$_2$O$_3$ and Fe$_3$O$_4$ in AMO. The amorphous-Al$_2$O$_3$ layer was deposited at room temperature. After the deposition of Al$_2$O$_3$, as shown in Fig. 2(c), the Si (7×7) streak pattern turned into a halo pattern, which indicated that the Al$_2$O$_3$ layer was amorphous. Figure 2(d) shows the RHEED pattern of Fe$_3$O$_4$ on the amorphous-Al$_2$O$_3$. A ring and streak pattern was observed, which implied the presence of a polycrystalline surface. Thus, the epitaxial γ-Al$_2$O$_3$ played a crucial role in the formation of epitaxial Fe$_3$O$_4$ on the Si substrate.

Figure 2(e) and (f) show the RHEED pattern of the Si substrate and Fe$_3$O$_4$ in W/O. The surface of the Si substrate exhibited a diffused streak pattern owing to the introduction of oxygen gas, which oxidized the Si surface. In Fig. 2(f), the RHEED pattern of Fe$_3$O$_4$ on SiO$_x$ shows a halo pattern, which indicated that spinel-type Fe$_3$O$_4$ was not formed.
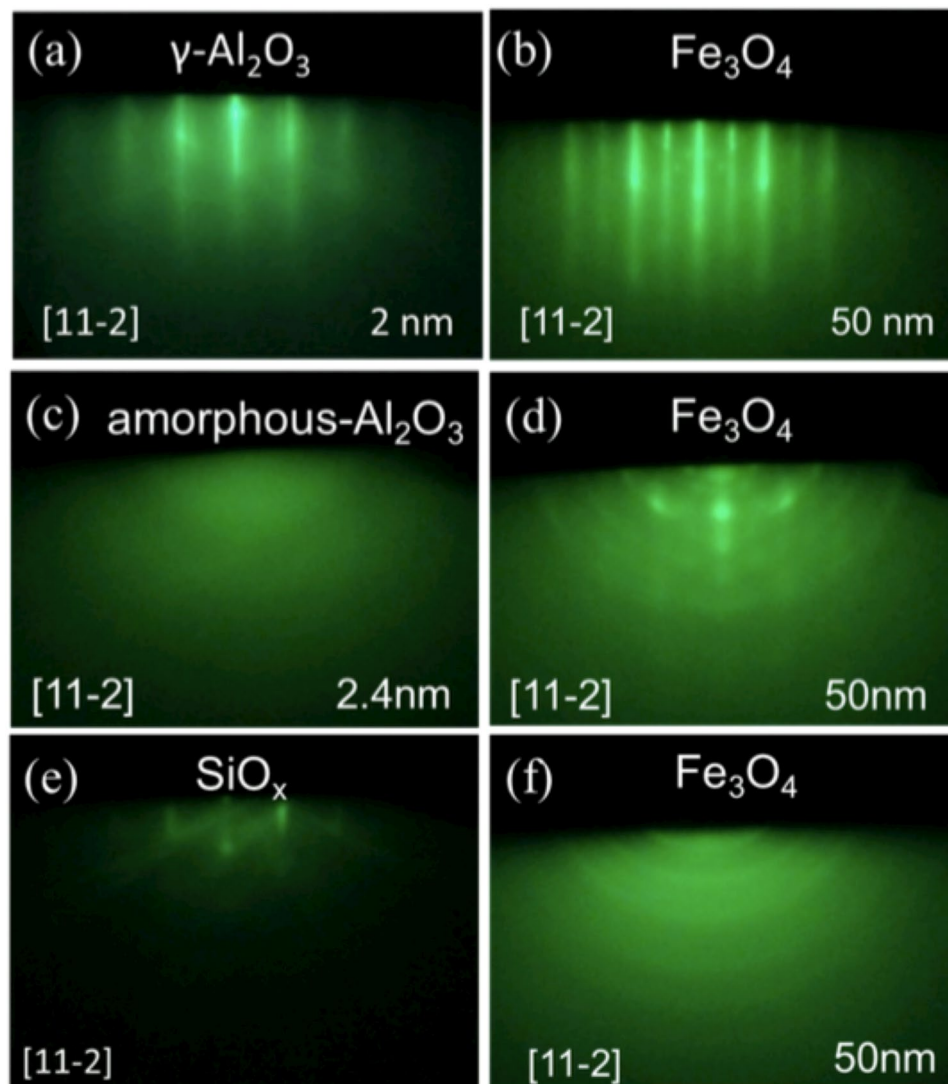
Figure 2. RHEED patterns: (**a**) γ-Al$_2$O$_3$ and (**b**) Fe$_3$O$_4$ film on γ-Al$_2$O$_3$ in EPI, (**c**) amorphous-Al$_2$O$_3$ and (**d**) Fe$_3$O$_4$ on amourphous-Al$_2$O$_3$ in AMO, (**e**) Si surface before depositing Fe$_3$O$_4$, and (**f**) Fe$_3$O$_4$ on Si substrate in W/O.

X-ray diffraction.   To confirm the crystallization, the θ–2θ X-ray diffraction (XRD) measurements were carried out on three samples, as shown in Fig. 3(a). The diffraction pattern of Fe$_3$O$_4$ on an γ-Al$_2$O$_3$ buffer layer in EPI (red line) exhibited four peaks (18.3°, 37.2°, 57.2°, 79.4°), which were in agreement with the diffraction patterns of Fe$_3$O$_4$ (111), (222), (333) and (444) planes. This indicated that the Fe$_3$O$_4$ film was (111)-oriented without other orientations or phases. The lattice constant measured by XRD was estimated to be 8.39 Å. The lattice constant of the in-plane direction was estimated to be 8.23 Å (Supplementary Fig. S3), which is smaller than the bulk lattice parameter. Therefore, the Fe$_3$O$_4$ was considered to be compressed in-plane.

To investigate the in-plane epitaxial relationship, we conducted φ-scan measurements of Si(311) and Fe$_3$O$_4$ (4-40), as shown in Fig. 3(b). The six peaks of Fe$_3$O$_4$ (4-40) appeared at 60° intervals, indicating the presence of two 180° rotated domains in the Fe$_3$O$_4$ layer. The epitaxial relationships were [11-2]Fe$_3$O$_4$(111) and [-1-12] Fe$_3$O$_4$(111) parallel to [11-2]Si(111), as exhibited in Fig. 3(c). In addition, the peaks of the Fe$_3$O$_4$ film were broader than that of the Si substrate. There was a lattice mismatch of 5.7% at γ-Al$_2$O$_3$/Fe$_3$O$_4$.

The θ–2θ XRD diffraction pattern of Fe$_3$O$_4$ in AMO (blue line) exhibited four peaks, which was identical with the diffraction pattern of Fe$_3$O$_4$ in EPI. Therefore, the Fe$_3$O$_4$ in AMO was also (111)-oriented. However, the RHEED pattern in Fig. 1(d) implied the presence of a polycrystalline structure. Furthermore, the Fe$_3$O$_4$(4-40) diffraction peak was not observed in the φ-scan measurement. Therefore, we concluded that the Fe$_3$O$_4$ had a textured structure and the growth direction was (111).

The θ–2θ XRD diffraction pattern of Fe$_3$O$_4$ in W/O (green line) exhibited small peaks related to Fe$_3$O$_4$(311), (400), (422) and unknown peaks. In a previous study[30], the XRD of Fe$_3$O$_4$ on SiO$_2$ indicated that the Fe$_3$O$_4$ layer was polycrystalline and contained other phases.
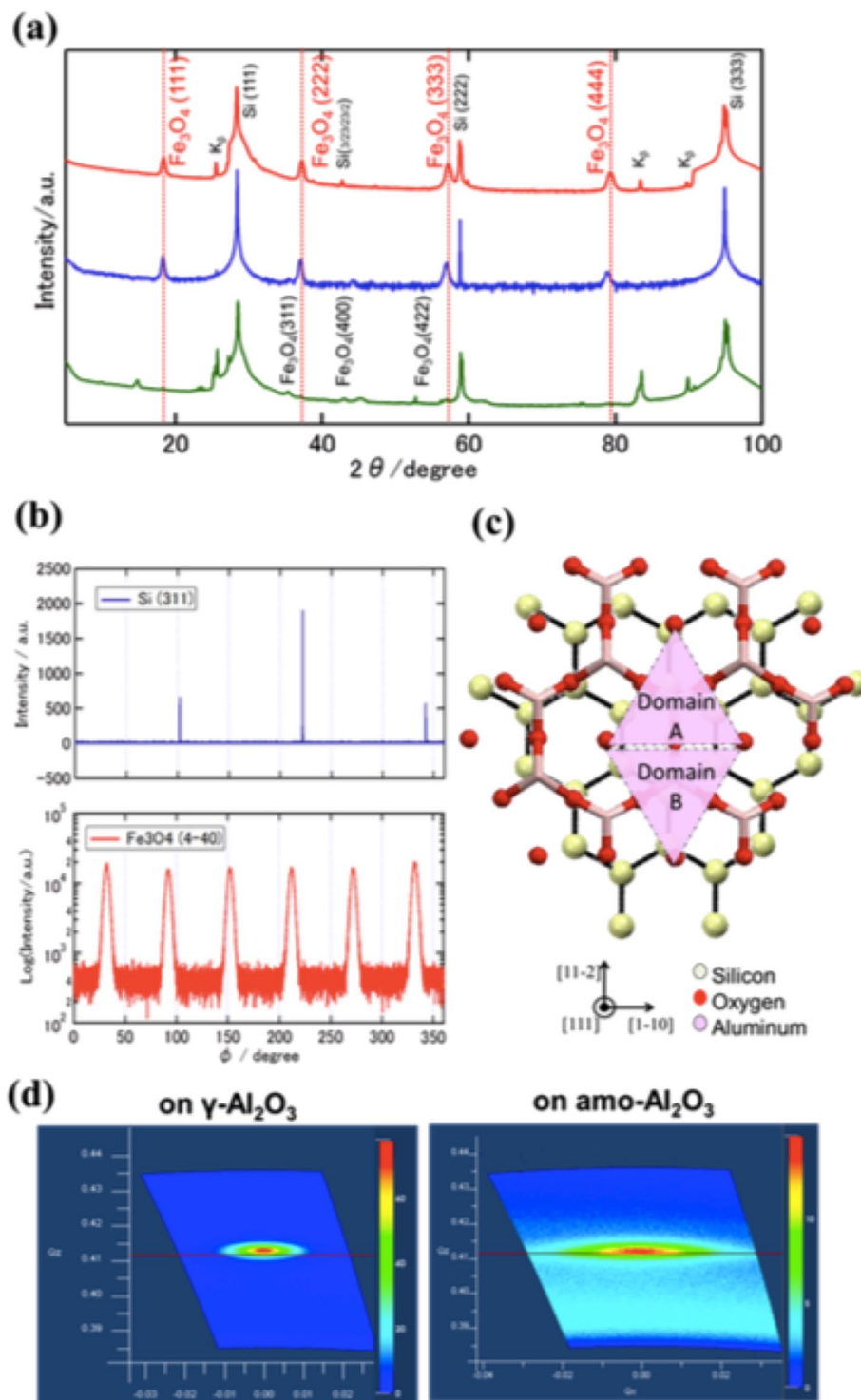
Figure 3. X-Ray diffraction: (**a**) θ-2θ XRD profiles, (**b**) φ-scan measurement, (**c**) Epitaxial relationship between Si and γ-Al$_2$O$_3$, (**d**) X-ray reciprocal space maps of Fe$_3$O$_4$ on γ-Al$_2$O$_3$ in EPI and Fe$_3$O$_4$ on amo-Al$_2$O$_3$ in AMO.

To investigate the crystallinity of the Fe$_3$O$_4$ layer in detail, we carried out X-ray reciprocal space mapping around the symmetric (222) diffraction for Fe$_3$O$_4$ in EPI and AMO (Fig. 3(d)). The symmetrical scan showed that the Fe$_3$O$_4$(222) spot on amorphous-Al$_2$O$_3$ was larger than the Fe$_3$O$_4$ spot on γ-Al$_2$O$_3$, which means that the Fe$_3$O$_4$ in AMO had an angle distribution in the growth directions. Although the reason for the (111) oriented Fe$_3$O$_4$ growth on amorphous-Al$_2$O$_3$/Si(111) was unclear, two possibilities exist that could explain this growth. The first is a reduction in the total anisotropy energy related to the surface energy and interface energy[31]. The difference between AMO and W/O could be attributed to the difference of the surface and interface energy of amo-Al$_2$O$_3$
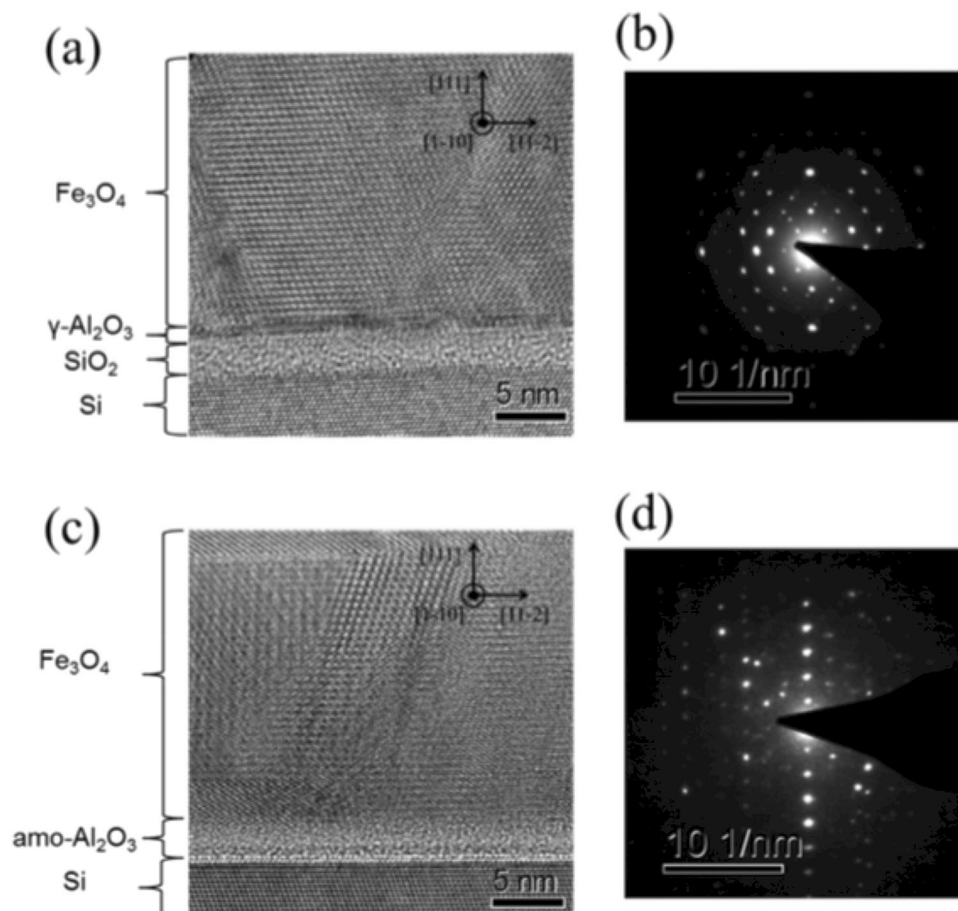
Figure 4. TEM observation: (**a**) Cross-section TEM image and (**b**) electron diffraction pattern of Si(111)/γ-Al_2O_3/Fe_3O_4 in EPI taken along the [1-10] axis zone, (**c**) Cross-section TEM image and (**d**) electron diffraction of Si(111)/amo-Al_2O_3/Fe_3O_4 in AMO taken along the [1-10] axis zone.

and amo-SiO. The second possibility is that the amo-Al_2O_3 maintains a crystal structure of Si locally because the amo-Al_2O_3 layer was very thin. Fe_3O_4 could utilize such a microcrystal-like region as a growth nucleus.

Transmission electron microscope observation. We conducted cross-sectional transition electron microscopy (TEM) analysis to confirm the crystallinity and compositions of the materials. Figure 4 shows the cross-section TEM images in which the electron beams were incident along the Si [1-10] zone axis. In Fig. 4(a), the TEM image shows that the Fe atoms of Fe_3O_4 were orderly aligned; thus, the Fe_3O_4 film was epitaxial. The electron diffraction (ED) of Fe_3O_4 in EPI shown in Fig. 4(b) was in good agreement with the simulation of spinel structure. The left side in Fig. 4(a) shows the epitaxial relationship on [11-2]Fe_3O_4(111)/[11-2]Si(111), whereas the center of image shows the epitaxial relationship on [-1-12]Fe_3O_4(111)/[11-2]Si(111), which were consistent with the results of the ϕ-scan measurements in the XRD. In addition, the spacing of the (111) planes were estimated at 4.87 Å from the high angle annular dark-field scanning (HAADF) image (Supplementary Fig. S4(c)), which were almost the same as the out-of-plane lattice constant (4.84 Å) determined by XRD in Fig. 3(a) and that of bulk Fe_3O_4 (4.85 Å). In contrast, the TEM image of Fe_3O_4 in AMO shown in Fig. 4(c) demonstrated that the structure was polycrystalline and grain boundaries were clearly observed. The ED image in Fig. 4(d) consisted of the diffraction from the grains with some crystal orientations. In the low magnification TEM image (supplementary Fig. S4(b)), some grains with a size of 15–30 nm appeared.

With respect to the buffer layer, the thickness of γ-Al_2O_3 was estimated from the HRTEM image (Fig. 4(a)) to be approximately 1 nm, which was thinner than the nominal value measured by the crystal oscillator in the chamber. The reason for this difference in thickness was unclear; however, it could be due to the fluctuation of the crystal oscillator or re-evaporation of Al_2O_3 because the γ-Al_2O_3 was grown at a high temperature (900 °C). We could see the amorphous layer under the γ-Al_2O_3 layer, which was determined to be a SiO_x layer by HAADF and Energy dispersive X-ray spectroscopy (EDS) mapping images (Fig. 5). The SiO_x layer was considered to form during the growth of Fe_3O_4 because the Fe_3O_4 was grown in 4×10^{-4} Pa O_2 gas. It was reported that Si was oxidized through the γ-Al_2O_3 layer of less than 2.0 nm by introducing oxygen ($>10^{-3}$ Pa)[32]. To confirm that, we fabricated a γ-Al_2O_3 (7.5 nm) film on Si(111), and carried out XRD and TEM observations (supplementary Fig. S5(a) and (b)). The γ-Al_2O_3 grew epitaxially on Si and we found no amorphous layer at the Si(111)/γ-Al_2O_3(7.5 nm) interface.
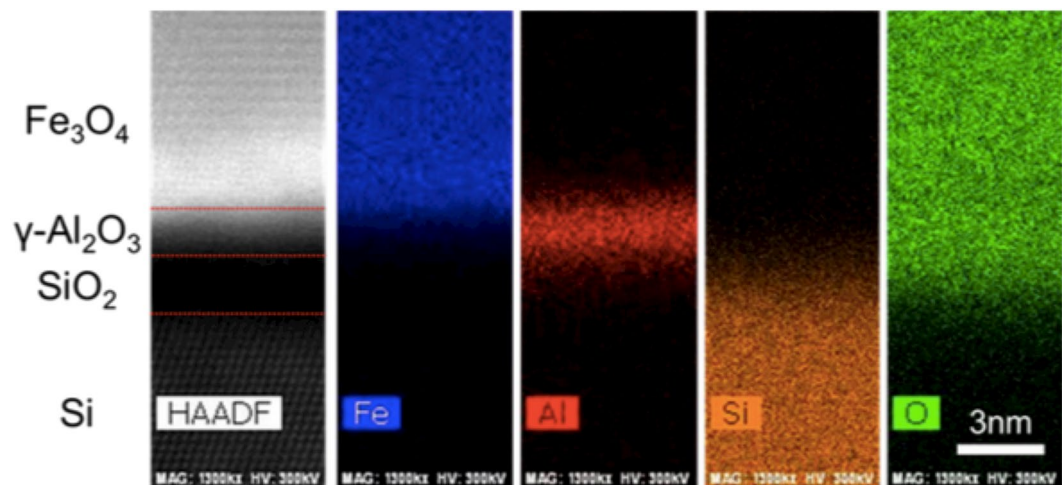
Figure 5. The EDS mapping of the heterostructure: From the left image, HAADF image, EDS mapping of Fe, Al, Si, and O.
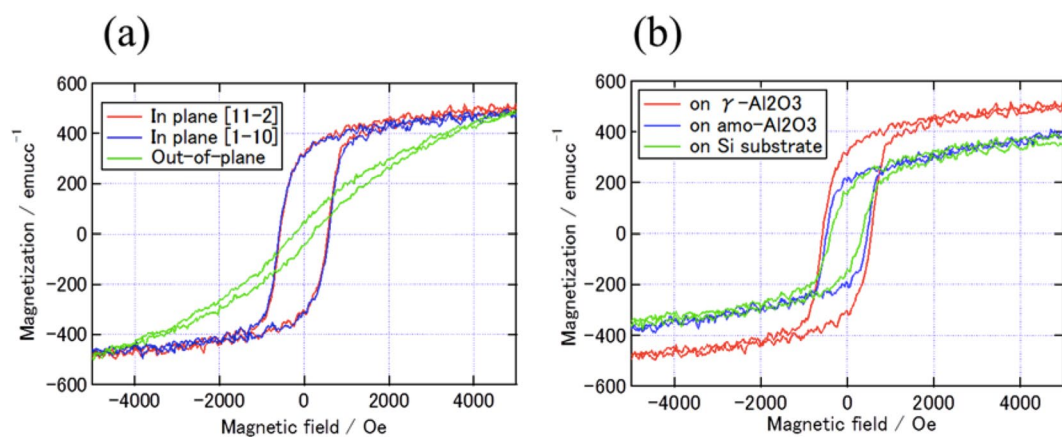

Figure 6. Magnetic properties (**a**) Magnetization curves of Fe_3O_4 on γ-Al_2O_3 in the magnetic field along [11-2], [1-10], and out of plane [111] (**b**) Magnetization curves of EPI, AMO, and W/O in the magnetic field along [11-2].

Magnetic characteristics.   The magnetic character of Fe_3O_4 is one of its fundamental properties. The magnetization curves at room temperature for the Fe_3O_4 films on γ-Al_2O_3 layer are shown in Fig. 6(a). The directions of the magnetic field were in-plane [11-2], in-plane [1-10] and out-of-plane [111]. The hysteresis curve along [11-2] was the same as that along [1-10] and the Fe_3O_4 film had in-plane magnetization. The saturation magnetization (M_s) was 480 emu/cm^3 for all magnetic field directions. The remanent magnetization (M_r), the coercive field (H_c), and the remanent ratio (M_r/M_s) in the in-plane field were 280 emu/cm^3 500 Oe, and 0.48, respectively, and those for the out-of-plane field were 47 emu/cm^3, 225 Oe, and 0.08, respectively. The hysteresis loops for Fe_3O_4 in EPI, AMO, and W/O are illustrated in Fig. 6(b). Fe_3O_4 in EPI had the largest H_c and M_s among the three samples. The M_s of Fe_3O_4 in EPI was the same as the value of bulk Fe_3O_4. Although the reason for small magnetization for AMO and W/O has not been clear so far, the antiphase boundary or disordered structure at grain boundary could be responsible for it[33, 34].

Transport characteristics.   Figure 7 shows that the dependence of the resistance on temperature for the Fe_3O_4 film in EPI. As is well-known, Fe_3O_4 is an electric conductor at room temperature and the resistivity increases exponentially with decreasing temperature. The resistivity of the film at 300 K was 2.5×10^{-4} Ωcm, which is lower than the bulk value (5×10^{-3} Ωcm)[35]. The dlogR/dT plots (inset) show a valley at approximately 120 K. This anomaly corresponds to a Verwey transition[36], which is a famous phase transition in Fe_3O_4. The Verwey transition has been reported to sharply change the resistivity by approximately one digit[37]; however, the transition is easily disappeared by impurities or structure defects[34, 38]. As the Fe_3O_4 in EPI possessed magnetic and electric characteristics that were comparable to bulk Fe_3O_4, the Fe_3O_4 on γ-Al_2O_3 buffer layer was very good quality.
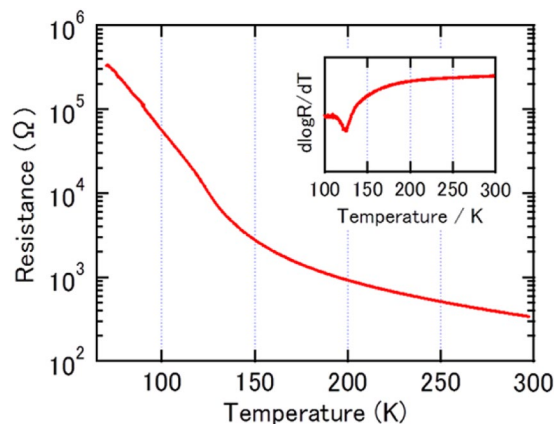
Figure 7. Transport properties: The resistivity of Si(111)/γ-Al$_2$O$_3$/Fe$_3$O$_4$ as a function of temperature. The inset is dlogR/dT plot.

Conclusions

We fabricated an epitaxial Fe$_3$O$_4$ film on a Si substrate by inserting an γ-Al$_2$O$_3$ buffer layer. From the XRD measurement and TEM observation, the γ-Al$_2$O$_3$ buffer layer contributed to the growth of epitaxial Fe$_3$O$_4$(111) on Si(111). In contrast, the Fe$_3$O$_4$ film on an amo-Al$_2$O$_3$ buffer layer had an (111)-orientation with a textured structure. The Fe$_3$O$_4$ on γ-Al$_2$O$_3$ had magnetic properties corresponding to the bulk Fe$_3$O$_4$, furthermore the resistivity exhibited a Verwey transition at 120 K. The results indicate that the heterostructure of Si substrate/γ-Al$_2$O$_3$/Fe$_3$O$_4$ could be used as a part of magnetic tunnel junctions or spin injection devices and will allow us to integrate spintronic devices including Fe$_3$O$_4$ electrode, e.g., spin-FET or magnetic tunnel junctions, on Si.

Methods

Preparation of the samples.   Before deposition, the Si substrate was cleaned by a standard Radio Corporation of America clean[39] and hydrofluoric (HF) acid solution and annealed at 900 °C under a vacuum of $< 10^{-6}$ Pa[29]. The γ-Al$_2$O$_3$ buffer layer was formed by evaporating the Al$_2$O$_3$ source material at 900 °C and annealing at 900 °C for 30 minutes. In previous reports, γ-Al$_2$O$_3$ was grown at >850 °C and under a vacuum of $< 10^{-6}$ Pa[40]. The growth conditions we used for γ-Al$_2$O$_3$ were in the range of the report. In Si(111)/amo-Al$_2$O$_3$/Fe$_3$O$_4$, the amo-Al$_2$O$_3$ was grown at room temperature under a vacuum of $< 3 \times 10^{-6}$ Pa. Then, the Fe$_3$O$_4$ film was formed by reactive deposition at 300 °C under a O$_2$ atmosphere of 4.0×10^{-4} Pa[41]. All the samples were fabricated under the same growth conditions to investigate the dependence of the quality of Fe$_3$O$_4$ films on the buffer layer.

Measurements.   The epitaxial growth and crystal structure were confirmed by RHEED, XRD (Rigaku SmartLab (9 kW)), and TEM (FEI Titan3 G2 60-300). Cross-sectional samples for TEM were prepared by using conventional mechanical polishing and dimpling techniques[42]. The magnetic properties of Fe$_3$O$_4$ were measured by vibrating sample magnetometer (VSM) and the electrical properties were measured by direct current (DC) measurements.

References

1. Jedema, F. J., Heersche, H. B., Filip, A. T., Baselmans, J. J. A. & van Wees, B. J. Electrical detection of spin precession in a metallic mesoscopic spin valve. *Nature* **416**, 713–716 (2002).
2. van't Erve, O. M. J. *et al*. Electrical injection and detection of spin-polarized carriers in silicon in a lateral transport geometry. *Appl. Phys. Lett.* **91**, 212109 (2007).
3. Dash, S. J., Sharma, S., Patel, R. S., de Jong, M. P. & Jansen, R. Electrical creation of spin polarization in silicon at room temperature. *Nature* **462**, 491–494 (2009).
4. Datta, S. & Das, B. Electronic analog of the electro-optic modulator. *Appl. Phys. Lett.* **56**, 665 (1990).
5. Sugahara, S. & Tanaka, M. A spin metal–oxide–semiconductor field-effect transistor using half-metallic-ferromagnet contacts for the source and drain. *Appl. Phys. Lett.* **84**, 2307 (2004).
6. Sasaki, T. *et al*. Electrical Spin Injection into Silicon Using MgO Tunnel Barrier. *Appl. Phys. Exp.* **2**, 053003 (2009).
7. Johnson, M. & Silsbee, R. H. Interfacial charge-spin coupling: Injection and detection of spin magnetization in metals. *Phys. Rev. Lett.* **55**, 1790 (1985).
8. Sasaki, T. *et al*. Spin Transport in Nondegenerate Si with a Spin MOSFET Structure at Room Temperature. *Phys. Rev. Applied* **2**, 034005 (2014).
9. Ohishi, M. *et al*. Spin Injection into a Graphene Thin Film at Room Temperature. *Jpn. J. Appl. Phys.* **46**, L605–L607 (2007).
10. Shiraishi, M. *et al*. Robustness of Spin Polarization in Graphene-Based Spin Valves. *Adv. Funct. Mater.* **19**, 3711 (2009).
11. Bibes, M. & Barthélémy, A. Oxide spintronics. *IEEE Trans. Electron Devices* **54**, 1003 (2007).
12. Yanagihara, H., Utsumi, Y., Niizeki, T., Inoue, J. & Kita, E. Perpendicular magnetic anisotropy in epitaxially strained cobalt-ferrite (001) thin films. *J. Appl. Phys.* **115**, 17A719 (2014).
13. Takaobushi, J., Kanki, T., Kawai, T. & Tanaka, H. Preparation of ferroelectric field effect transistor based on sustainable strongly correlated (Fe,Zn)$_3$O$_4$ oxide semiconductor and their electrical transport properties. *Appl. Phys. Lett.* **98**, 102506 (2011).
14. Niizeki, T. *et al*. Observation of longitudinal spin-Seebeck effect in cobalt-ferrite epitaxial thin films. *AIP Advances* **5**, 053603 (2015).
15. Yanase, A. & Shiratori, K. Band Structure in the High Temperature Phase of Fe$_3$O$_4$. *J. Phys. Soc. Jpn.* **53**, 312 (1984).
16. Ramos, A. V. *et al*. Room temperature spin filtering in epitaxial cobalt-ferrite tunnel barriers. *Appl. Phys. Lett.* **91**, 122107 (2007).
17. Santos, T. S. & Moodera, J. S. Observation of spin filtering with a ferromagnetic EuO tunnel barrier. *Phys. Rev. B* **69**, 241203 (2004).
18. Takahashi, Y. K. *et al*. High spin-filter efficiency in a Co ferrite fabricated by a thermal oxidation. *Appl. Phys. Lett.* **96**, 072512 (2010).

19. Li, P. *et al*. Ultrathin Epitaxial Ferromagnetic γ-Fe$_2$O$_3$ Layer as High Efficiency Spin Filtering Materials for Spintronics Device Based on Semiconductors. *Adv. Funct. Mater.* **26**, 5679–5689 (2016).
20. Li, P. *et al*. Spin Filtering in Epitaxial Spinel Films with Nanoscale Phase Separation. *ACS Nano* **11**, 5011–5019 (2017).
21. Ziese, M., Köhler, U., Bollero, A., Höhne, R. & Esquinazi, P. Schottky barrier and spin polarization at the Fe$_3$O$_4$-Nb:SrTiO$_3$ interface. *Phys. Rev. B* **71**, 180406R (2005).
22. Watanabe, H., Fujita, K. & Ichikawa, M. Thermal decomposition of ultrathin oxide layers on Si(111) surfaces mediated by surface Si transport. *Appl. Phys. Lett.* **70**, 1095 (1997).
23. Senn, M. S., Wright, J. P. & Attfield, J. P. Charge order and three-site distortions in the Verwey structure of magnetite. *Nature* **481**, 173–176 (2012).
24. Mi, W., Guo, Z., Wang, Q., Yang, Y. & Bai, H. Charge ordering in reactive sputtered (100) and (111) oriented epitaxial Fe$_3$O$_4$ films. *Scripta Materialia* **68**, 972–975 (2013).
25. Liu, X., Yin, L. & Mi, W. Biaxial strain effect induced electronic structure alternation and trimeron recombination in Fe$_3$O$_4$. *Sci. Rep.* **7**, 43403 (2017).
26. Dedkov, Y. S., Rüdiger, U. & Güntherodt, G. Evidence for the half-metallic ferromagnetic state of Fe$_3$O$_4$ by spin-resolved photoelectron spectroscopy. *Phys. Rev. B* **65**, 064417 (2002).
27. Merckling, C. *et al*. Growth of crystalline γ-Al$_2$O$_3$ on Si by molecular beam epitaxy: Influence of the substrate orientation. *J. Appl. Phys.* **102**, 024101 (2007).
28. Jung, Y. C., Miura, H. & Ishida, M. Formation of Very Thin Epitaxial Al$_2$O$_3$ Pre-layer with Very Smooth Surface on Si (111) Using a Protective Oxide Layer. *Jpn. J. Appl. Phys.* **38**, 2333 (1999).
29. Merckling, C. *et al*. Epitaxial growth and relaxation of γ-Al$_2$O$_3$ on silicon. *Thin Solid Films* **515**, 6479–6483 (2007).
30. Park, C. *et al*. Interfacial composition and microstructure of Fe$_3$O$_4$ magnetic tunnel junctions. *IEEE Trans. Magn.* **39**, 2806 (2003).
31. Shirsath, S. E., Liu, X., Yasukawa, Y., Li, S. & Morisako, A. Switching of magnetic easy-axis using crystal orientation for large perpendicular coercivity in CoFe$_2$O$_4$ thin film. *Sci. Rep.* **6**, 30074 (2016).
32. Bachelet, R. *et al*. Functional spinel oxide heterostructures on silicon. *Cryst. Eng. Comm.* **16**, 10741–10745 (2014).
33. Margulies, D. T. *et al*. Origin of the Anomalous Magnetic Behavior in Single Crystal Fe$_3$O$_4$ Films. *Phys. Rev. Lett.* **79**, 5162 (1997).
34. Mi, W. B., Shen, J. J., Jiang, E. Y. & Bai, H. L. Microstructure, magnetic and magneto-transport properties of polycrystalline Fe$_3$O$_4$ films. *Acta Materialia* **55**, 1919–1926 (2007).
35. Eerenstein, W., Palsra, T. T., Hibma, T. & Celotto, S. Origin of the increased resistivity in epitaxial Fe$_3$O$_4$ films. *Phys. Rev. B* **66**, 201101(R) (2002).
36. Verwey, E. J. W. Electronic Conduction of Magnetite (Fe$_3$O$_4$) and its Transition Point at Low Temperatures. *Nature* **144**, 327–328 (1939).
37. Kado, T., Saito, H. & Ando, K. Room-temperature magnetoresistance in magnetic tunnel junctions with Fe$_3$O$_4$ electrode. *J. Appl. Phys.* **101**, 09J511 (2007).
38. Tsuda, N. *et al. Electronic Conduction in Oxide* (Springer, Berlin-Heidelberg, 2000)
39. Kern, W. & Puotinen, D. Cleaning solutions based on hydrogen peroxide for use in silicon semiconductor technology. *RCA Review* **31**, 187–206 (1970).
40. Wu, S. Y. *et al*. High-quality thin single-crystal γ-Al$_2$O$_3$ films grown on Si(111). *Appl. Phys. Lett.* **87**, 091908 (2005).
41. Nagahama, T. *et al*. Magnetic properties of epitaxial Fe$_3$O$_4$ films with various crystal orientations and tunnel magnetoresistance effect at room temperature. *Appl. Phys. Lett.* **105**, 102410 (2014).
42. Lari, L., Lea, S., Feeser, C., Wessels, B. W. & Lazarov, V. K. Ferromagnetic InMnSb multi-phase films study by aberration-corrected (scanning) transmission electron microscopy. *J. Appl. Phys.* **111**, 07C311 (2012).

Acknowledgements

Author Contributions

N.T. and T.N. conceived and designed the experiments using the help of other authors. N.T., T.N., Y.Y., T.Y. and T.S. performed the sample preparation, XRD measurements, magnetic and electrical measurements. T.H., A.H., N.T. and T.N. performed TEM observations. All the authors contributed to analysing and interpreting the data, and to writing the manuscript.

Additional Information

Supplementary information accompanies this paper at doi:10.1038/s41598-017-07104-z

Competing Interests: The authors declare that they have no competing interests.

Publisher's note: Springer Nature remains neutral with regard to jurisdictional claims in published maps and institutional affiliations.